

Thiourea Treatment to Boost the Electrochemical Kinetics and Interfacial Stability of MnCo₂O_{4.5} Spinel as a Novel Bifunctional Electrocatalyst for Rechargeable Zn–Air Batteries

Wei Zhao, Jiaxing Yan, Zijian Wang, and Yifeng Zheng*

Developing efficient and cost-effective bifunctional catalysts is pivotal in advancing Zn–air batteries (ZABs). In this study, a novel multiple-surface modification strategy is presented for MnCo₂O_{4.5} (MCO) spinel electrocatalyst with the pyrolysis of thiourea. The preparation involves a hydrothermal process to obtain MCO, followed by surface modification with varying concentrations of thiourea (10% weight (wt), 30, 50%wt) under nitrogen atmosphere at 300 °C. The 10% wt thiourea-modified MCO (MCO-10%T) achieves a half-wave potential of 0.787 V vs. reversible hydrogen electrode for the oxygen reduction reaction and an overpotential of 450 mV at 10 mA cm⁻² for the oxygen evolution reaction, rivaling the benchmark Pt/C-RuO₂ catalyst. This enhanced performance

arises from the synergistic effects of sulfur doping, carbon coating, and the hierarchical porous structure introduced by thiourea. These features collectively improve electrical conductivity, increase active site availability, and facilitate charge transfer. When employed as an air cathode catalyst for aqueous ZABs, MCO-10%T demonstrates a high specific capacity of 800 mAh g⁻¹, a power density of 154 mW cm⁻², and outstanding charge–discharge cycling stability. This study offers important guidance for designing bifunctional catalysts with enhanced activity and stability, leveraging surface reconstruction strategies tailored for spinel materials.

1. Introduction

Developing clean vitality sources to diminish the dependence on conventional fossil fuels is basic in relieving natural contamination, combating climate alter, and tending to the vitality emergency.^[1–4] Zinc–air batteries (ZABs) have great promise because of their favorable environmental effects, high energy density, security, and low cost.^[5,6] Oxygen evolution reaction (OER) and oxygen reduction reaction (ORR) are key to the operation of ZABs.^[7] OER and ORR involve complex mechanisms and exhibit sluggish kinetics.^[7–9] These challenges significantly limit the activity of ORR and OER. The distinct optimal adsorption energies required for ORR and OER necessitate different ideal active sites for each reaction.^[10,11] For example, though Pt-based materials are viewed as cutting edge impetuses for ORR,^[12,13] Conversely, catalysts like IrO₂ and RuO₂, which are profoundly productive for OER, demonstrate poor performance for ORR.^[14] Despite the excellent catalytic activity of Pt/C and RuO₂, their scarcity and high cost present significant challenges for the large-scale industrial application of these precious metals in electrocatalysis.^[15] Progressing cost-effective, effective, and strong

electrocatalysts for both OER and ORR is pivotal for the improvement of ZABs.

Given these restrictions, there's an urgent have to be create non-precious metal bifunctional catalysts that can improve both ORR and OER execution, subsequently overcoming the sluggish kinetics and high overpotential associated with ZABs. Transition metal spinel oxides (AB₂O₄) are emerging as the promising bifunctional catalysts due to their unique electron configurations, tunable active sites, low cost, high abundance, low toxicity, and versatile properties.^[16,17] In typical spinel structures, A²⁺ and B³⁺ ions occupy tetrahedral and octahedral sites within the O²⁻ ionic framework, respectively.^[16,17] The incomplete filling of the transition metal 3d orbitals comes about variable valence states and redox stability, which are impacted by the presence of unpaired electrons in their electronic configurations. The electronic configuration and lattice distortions within the spinel structure strongly impact the OER/ORR performance of materials, with key factors including exposed sites, electron occupancy, and spin states. Furthermore, cobalt-based spinel transition metal oxides have demonstrated remarkable catalytic performance for both ORR and OER.^[18,19] The incorporation of trivalent and quadrivalent manganese (Mn) into these oxides further enhances ORR activity by facilitating the exchange of O and -OH, thus improving oxygen adsorption. MnCo₂O_{4.5} (MCO), which is cobalt-based bimetallic transition metal oxides with a spinel structure, have gained considerable attention for their diverse valence changes, synergistic effects among mixed metal cations, and improved specific capacity properties.^[18,19]

Experimental results, along with density functional theory (DFT) calculations, indicate that sulfur doping enhances the

W. Zhao, J. Yan, Z. Wang, Y. Zheng
College of Materials Science and Engineering
Nanjing Tech University
No. 30 Puzhu Road(S), Nanjing, Jiangsu 211816, P. R. China (People's Republic of China)
E-mail: zhengyifeng@njtech.edu.cn

 Supporting information for this article is available on the WWW under <https://doi.org/10.1002/batt.202500122>

ORR and OER performance while also stabilizing the material's structure.^[20] The S-doped CoMn_2O_4 spinel revealed that S doping altered the surface characteristics and electronic configuration of the material, enhancing the electrical conductivity and surface activity. DFT calculations indicated that sulfur doping increases the energy gap between Co and Mn, and the 3d-O 2p orbitals, thereby improving electrocatalytic activity.^[20] Similarly, S-doping LaCoO_3 alters the spin state of Co from low spin to high spin, enhancing its catalytic performance.^[21] In previous reports, carbon carriers are capable of enhancing the conductivity and augmenting the active site of the material. Xiang et al. reported the N-anchored carbon nanofibers (NCNFs) embedded within CoMn_2O_4 (CMO) using electrospinning has been fabricated.^[22] Charge transfer is facilitated by the strong contact between CMO and NCNFs, and overall stability is improved by the conductive carbon network, which shields CMO from aggregation and corrosion. Carbon nanotube-decorated spinel CuCo_2O_4 exhibits enhanced electrocatalytic activity due to the increased active surface area provided by the carbon support and the presence of additional catalytic sites.^[23] These results demonstrate that both S-doped and carbon significantly enhance ORR and OER activities.

In the present study, we developed a multiple-surface modification strategy based on the pyrolysis of thiourea. The findings indicate that MCO spinel modified with thiourea brings about more surface oxygen vacancies, optimizes the specific surface area, lowers the surface energy, and refines the electronic structure. Consequently, the catalytic activity of MCO spinel treated with thiourea is significantly improved, and it can be further utilized in potential bifunctional electrocatalysts for ZABs.

2. Experimental Section

MCO was synthesized using a hydrothermal method. Typically, 1 mmol of $\text{Mn}(\text{CH}_3\text{COO})_2 \cdot 4\text{H}_2\text{O}$ and 2 mmol of $\text{Co}(\text{NO}_3)_2 \cdot 6\text{H}_2\text{O}$ were dissolved in deionized water and stirred thoroughly. Then, 5 mmol of urea and 5 mmol of NH_4F were added, and the mixture was stirred until fully dissolved. The prepared clear solution was placed in an autoclave reactor and heated at 120 °C for 6 h. Then the precursor was purified by washing with alcohol and deionized water three times each to remove unreacted substances and impurities. The precursor was calcined for three hours at 400 °C after being dried for twelve hours at 90 °C in an oven.

To prepare the thiourea surface-modified product, MCO was mixed with 10, 30, and 50 wt% thiourea in 60 mL of deionized water.



Scheme 1. The synthetic procedure of the MCO-10%T material.

The dried samples were then placed in a quartz tube furnace and sintered under an N_2 atmosphere at 300 °C for 0.5 h, yielding products labeled as MCO-10%T, MCO-30%T, and MCO-50%T. The synthesis route for MCO-10%T is illustrated in Scheme 1.

3. Results and Discussion

3.1. Material Structure and Analysis

The XRD patterns of MCO and MCO-x%T ($x = 10, 30, 50$) catalysts are shown in Figure 1a. The XRD diffraction peaks of all samples correspond to the $\text{MnCo}_2\text{O}_{4.5}$ phase (JCPDS card No: 32-0297), confirming that thiourea treatment does not change spinel phases. The introduction of thiourea causes the main peak in the XRD pattern to shift slightly to a smaller angle. This shift happens since the ionic radius of S^{2-} is larger than that of O^{2-} , and the partial substitution of O atoms by S ions leads to lattice expansion, resulting in a negative shift of the diffraction peak. Compared to MCO, the peak intensity of the MCO-10%T catalyst slightly increases, which is likely due to the secondary calcination process that enhances the material's crystallinity. However, with further increases in thiourea content, the peak intensity and crystallinity decrease. This decline is attributed to the expansion of grain boundaries and the introduction of additional stress, leading to more defects and strain within the crystal structure.^[23–25]

The fourier-transform infrared spectroscopy (FTIR) patterns of MCO and MCO-10%T catalysts are shown in Figure 1b. FTIR analysis shows an absorption band at 1136.6 cm^{-1} corresponding to the $\text{S}=\text{O}$ vibration mode, confirming the possibility of S doping inside the lattice.^[26,27] The band at 1627.8, 1889 and 1287 cm^{-1} corresponds to the $\text{C}=\text{O}$ functional group, confirming the presence of carbon.^[28] Vibrations at 1418.2, 3357, 1642.3 and 3653.9 cm^{-1} represent -OH adsorbed in water on the catalyst surface. The characteristic absorption peaks at 957.1, 1435.9 and 1035.9 cm^{-1} are attributed to metal–oxygen bond stretching in metal oxides, which consistent with XRD results, further confirming the synthesis of MCO spinel.^[29] Raman spectroscopy was used to examine the graphitization and defect properties of MCO and MCO-10%T catalysts (Figure 1c). The peaks at 189, 485, 517, and 673 cm^{-1} corresponding to the F_{2g} , E_g , F_{2g} , and A_g modes of spinel crystals, respectively.^[30] These results are consistent with XRD and FTIR, confirming the spinel structures. Characteristic peaks at 1352 cm^{-1} (D band) and 1585 cm^{-1} (G band) were observed in MCO-10%T but not in MCO, further supporting the presence of carbon in the electrocatalyst. A balance between graphitization and flaws is shown by the $I_{\text{D}}/I_{\text{G}}$ ratio of MCO-10%T, which is roughly 0.97. This could improve electrical conductivity and provide more active spot.^[31]

The morphologies and surface structures of the synthesized MCO and MCO-10%T are presented in Figure 2a–d, respectively. Both materials exhibit porous architectures. Nanorod-like structures are interleaved, resulting in the formation of numerous micrometer-sized pores. These rod-like structures arise from the aggregation of particles, each of which contains micropores. SEM images reveal that MCO primarily exhibits a rod-like configuration, composed of numerous nanoparticles ≈ 1 micron in size. Upon the addition of thiourea, the length of the nanorods

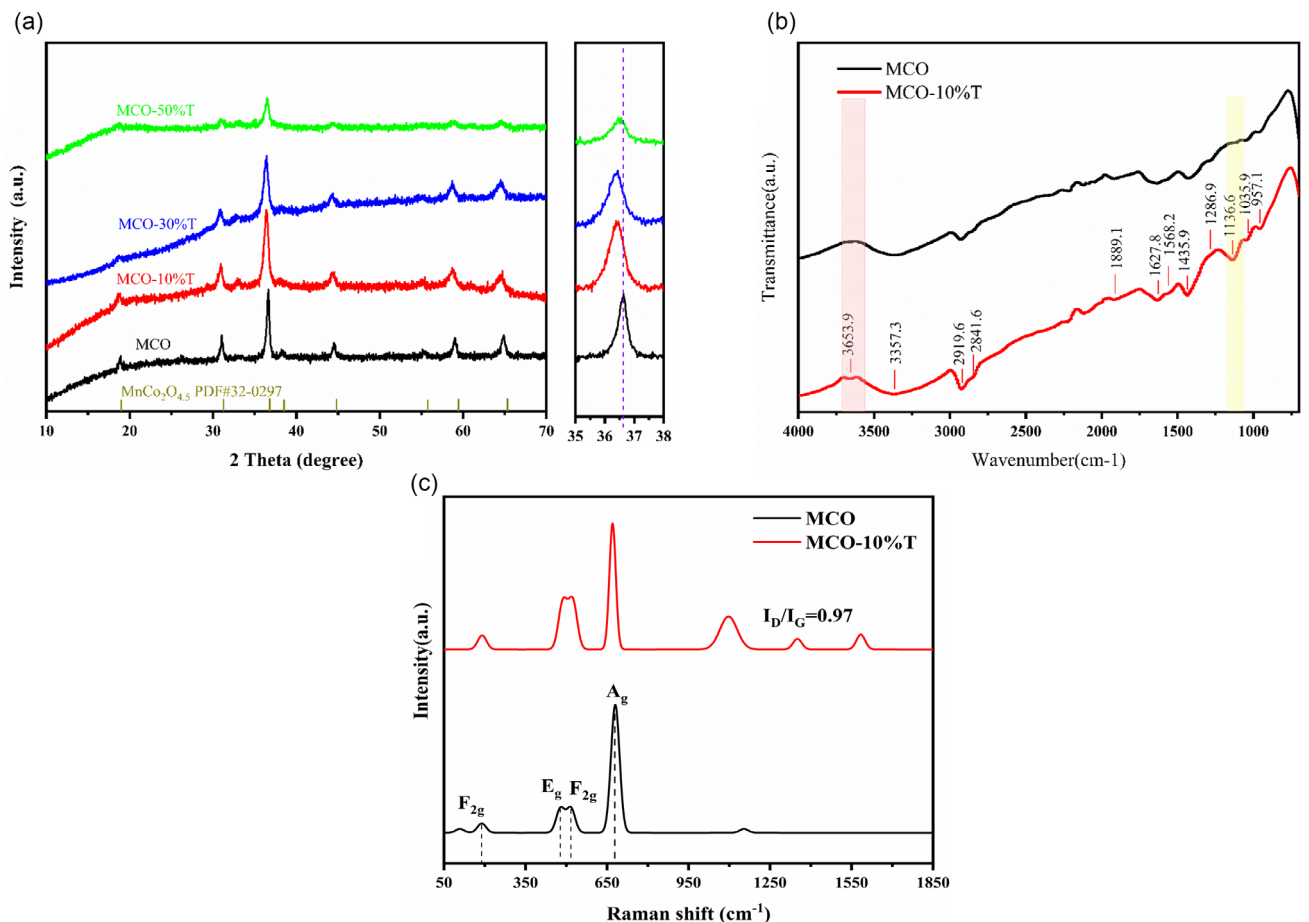


Figure 1. a) XRD patterns, b) the FT-IR spectra of MCO and MCO-10%T, and c) the Raman spectra of MCO and MCO-10%T.

decreases. And the closer bonding between the primary particles indicates that the material has a more stable surface structure. This modification increases the catalyst's specific surface area, offering more active sites for electrochemical reactions and facilitating the adsorption and desorption of oxygen-containing intermediates during the ORR and OER processes.^[31] As shown in Figure 2e, TEM images show MCO showing the rod-like structure. MCO-10%T still shows rod-like structure (Figure 2f). The high-resolution transmission electron microscopy (HRTEM) image (Figure 2g,h) shows the corresponding lattice fringes for MCO and MCO-10%T. The lattice spacing of 0.245 and 0.26 nm corresponds to the (311) crystal faces of MCO and MCO-10%T. For MCO-10%T, lattice fringes of 0.13 nm are shown, possibly corresponding to carbon. SEM-EDS analysis (see Figure S1, Supporting Information) confirms the uniform distribution of Mn, Co, O, C, and S elements within the MCO-10%T sample. It is proved that carbon is compounded on the surface of the material.

Moreover, WCA of the material, which is connected to surface energy, was utilized to assess its nanoscale surface properties.^[32] Figure 3a,b shows that MCO-10%T has a smaller WCA compared to MCO, showing that its surface dynamic destinations are more promptly available to oxygen atoms in water, subsequently improving the ORR response. In addition, the decreased surface vitality advances water adsorption on the cathode, possibly helping within the arrangement of dynamic intermediates favorable

to OER responses, driving to considerable changes in catalytic execution for both ORR and OER.^[32]

The surface area, pore volume and pore diameter of MCO and MCO-10%T were measured by BET (Figure 3c,d). The lack of an adsorption saturation plateau at high pressure near $P/P_0 = 1$ suggests that the prepared catalyst contains large pores, with MCO-10%T exhibiting the highest adsorption capacity in this region, indicative of its significant pore volume.^[33,34] The presence of macropores enhances full electrolyte contact with the catalyst, while the micropores and mesopores facilitate the desorption and dissociation of intermediates, thereby exposing more active sites.^[34,35] Additionally, the pore-size distribution of the prepared samples spans from 1–100 nm, as shown in Figure 3c,d, with multiple peaks, indicating a wide pore-size range and a hierarchical pore structure. In the BET surface area ($27.728 \text{ m}^2 \text{ g}^{-1}$) of MCO-10%T is larger than that of MCO ($18.672 \text{ m}^2 \text{ g}^{-1}$), MCO-30%T ($12.568 \text{ m}^2 \text{ g}^{-1}$) and MCO-50%T ($9.36 \text{ m}^2 \text{ g}^{-1}$). The pore volume of MCO-10%T at 5–20 nm is significantly higher than that of other samples, indicating that it has more mesoporous structure, which helps to improve oxygen diffusion and electrolyte penetration, and improve electrocatalytic performance. MCO and MCO-30%T also show a certain mesoporous structure, but the pore volume is small. MCO-50%T is mainly distributed in the larger pore-size range, and the overall pore volume is low, indicating that the pore structure is poor, which may not be conducive to catalytic reaction.

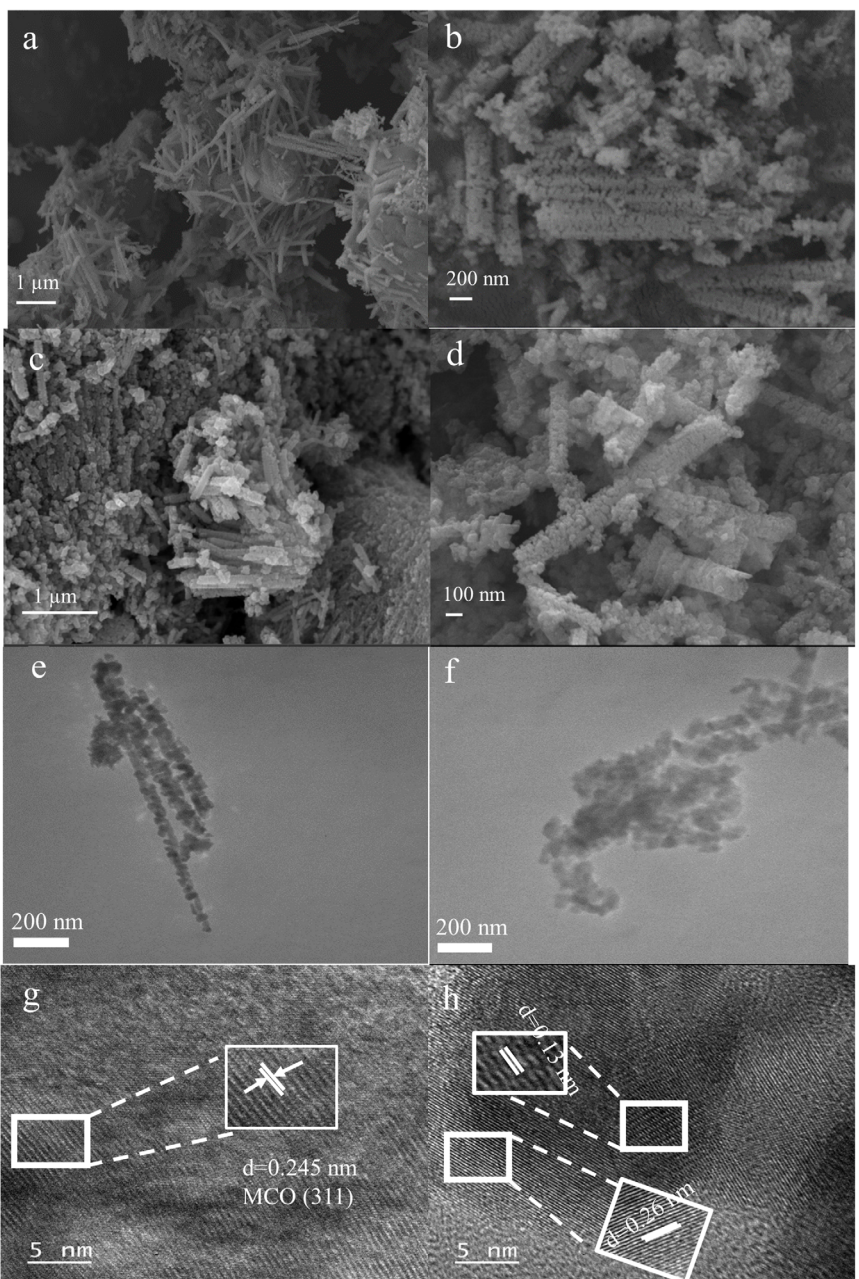


Figure 2. FE-SEM images of a,b) MCO, c,d) MCO-10%T; e) TEM image of MCO and f) TEM image of MCO-10%T; and g) HRTEM image of MCO; and h) HRTEM image of MCO-10%T.

X-ray photoelectron spectroscopy (XPS) was utilized to analyze the electronic arrangements and surface bonding states of MCO and MCO-10%T. The asymmetric Mn 2p spectra, featuring a spin-orbit splitting of 11.5 eV, display two peaks at 641.3 and 652.8 eV, corresponding to Mn 2p_{3/2} and Mn 2p_{1/2}, respectively.^[36,37] This dividing shows that Mn exists in blended valence states. Figure 4a shows that Mn²⁺ is answerable for the deconvoluted tops at 640.6 and 652.0 eV, Mn³⁺ is liable for those at 641.9 and 653.54 eV, and Mn⁴⁺ is liable for those at 643.8 and 654.8 eV. MCO-10%T has a bigger Mn⁴⁺/Mn³⁺ proportion (0.715) than MCO (0.52) (Table S1, Supporting Information), which is worthwhile for working on the ORR and OER execution.^[19,38] The Co 2p spectra of MCO and MCO-10%T show two twist circle

doublets, which relate to the low restricting energy Co 2p_{3/2} and the high restricting energy Co 2p_{1/2}, as displayed in Figure 4b. The concurrence of Co²⁺ and Co³⁺ blended valence states in the two impetuses are proposed by the ensuing parting of every one of these doublets into two pinnacles. Co³⁺ and Co²⁺ are credited to the tops at 779.4, 794.4 eV, and 780.3, 795.8 eV, individually. Two minor satellite pinnacles (assigned as "sat.") are found at 788.5 and 803.8 eV. For MCO, the Co³⁺/Co²⁺ relative electronic power proportion (0.65) is more modest than for MCO-10%T (0.78) (Table S2, Supporting Information). Co³⁺'s twist state speeds up electron move during the ORR and OER processes by working with the change from a low-twist to a moderate twist state.^[24] O1 (529.5 eV), O2 (531 eV), and O3 (532.3 eV) are the three pinnacles

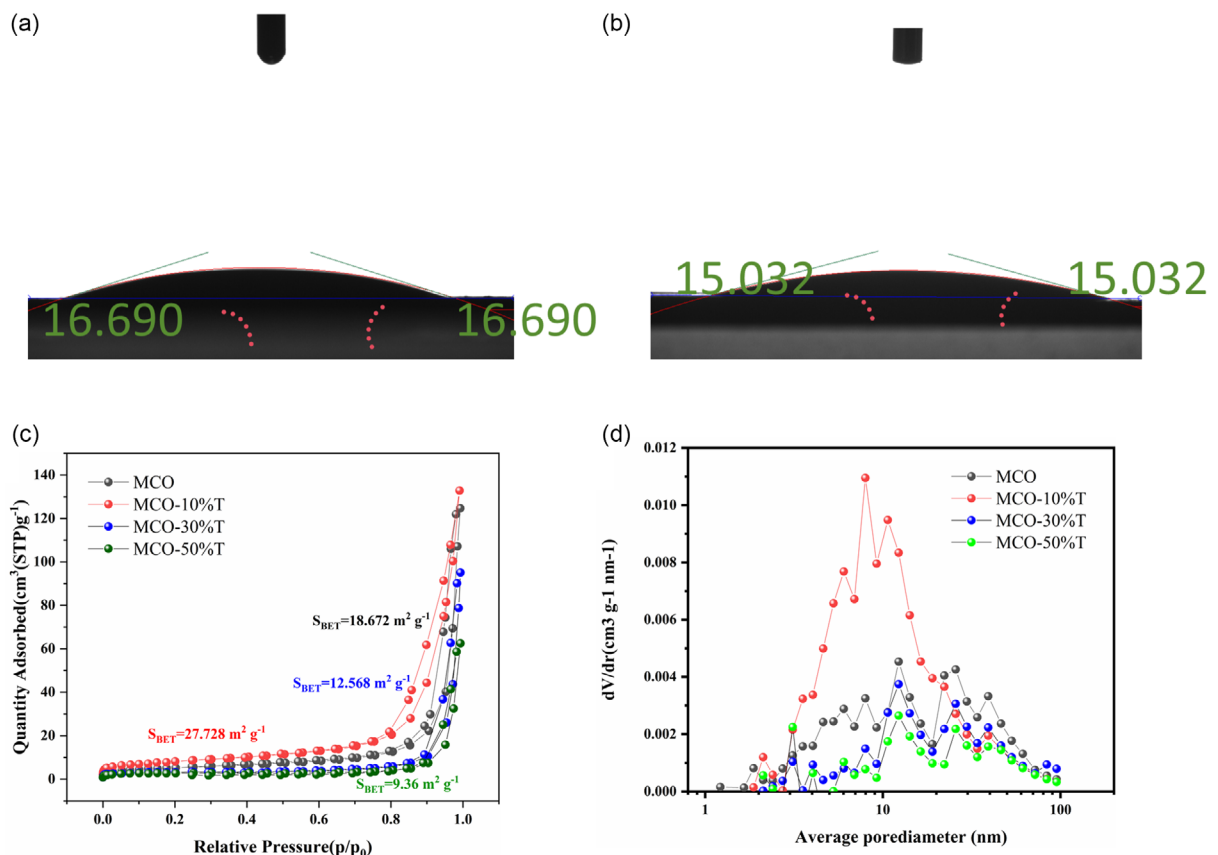


Figure 3. a) WCA of MCO and b) WCA of MCO-10%T; and c) N₂ adsorption–desorption isotherms; and d) pore-size distribution curves of the MCO and MCO-10%T, MCO-30%T and MCO-50%T.

that make up the O 1s spectra of MCO, as found in Figure 4c. These pinnacles relate to cross section oxygen, oxygen opportunity destinations, and surface-adsorbed oxygen, separately.^[37,39] The binding energy of Mn, Co, and O is decreased following the thioureide surface modification. This suggests that the incorporation of S²⁻ reduces the binding energy between metals and oxygen, primarily because sulfur (electronegativity 2.58) is less electronegative than oxygen (electronegativity 3.44). Consequently, the introduction of sulfur might cause neighboring transition metals (Mn and Co) to obtain more electron density, which would weaken the polarity and the bonding strength of M–O bonds, thereby facilitating the release of lattice oxygen and the formation of oxygen vacancies. Furthermore, the O₂/O₁ ratio for MCO-10%T (0.27) is higher than that for MCO, which may promote the formation of electronic holes and facilitate redox coupling (Table S3, Supporting Information). This, in turn, significantly enhances electrical conductivity and accelerates surface kinetics in catalytic reactions, thereby optimizing bifunctional catalytic activity.

As shown in Figure 4d, the electron paramagnetic resonance (EPR) signal increases with the increase of thiourea concentration. The results indicated that S doping has a notable regulatory effect on the electronic structure of MCO. Furthermore, the sulfur doping induces a positive charge on the metal sites, which enhances the bonding between the metal and hydroxyl groups. Appropriate oxygen vacancy was beneficial to ORR and OER performance. Consequently, MCO-10%T enhances catalytic performance by

facilitating the catalyst's reconfiguration to hydroxyl oxides during the OER process.

3.2. Electrochemical Measurements

Figure S2, Supporting Information illustrates the CV curves for MCO, MCO-10%T, MCO-30%T, MCO-50%T, and Pt/C-RuO₂ catalysts in 0.1 M KOH. All five catalysts exhibit a clear oxygen reduction peak, with MCO-10%T showing the highest peak among the MCO series catalysts, though slightly lower than Pt/C-RuO₂. This indicates that MCO-10%T has excellent ORR activity, approaching that of Pt/C-RuO₂.^[40] Figure 5a shows the half-wave potential of the MCO-10%T sample is 0.787 V versus reversible hydrogen electrode (RHE), which are higher than that of MCO-30%T (0.736 V), MCO (0.7025 V), and MCO-50%T (0.6175 V), only 53 mV difference from Pt/C-RuO₂ half-wave potential.^[41] The initial potential of MCO-10%T at -0.1 mA cm^{-2} is 0.912 V, approaching the level of Pt/C-RuO₂ (0.986 V) and surpassing that of MCO (0.9 V), MCO-30%T (0.88 V), and MCO-50%T (0.835 V). These findings suggest that the synergistic effects of S doping, with its higher electronegativity, combined with the presence of micropores, mesoporous structures, macroporous multistage pores, and carbon, play a crucial role in enhancing ORR activity.

Additionally, the Tafel slope for MCO-10%T is 110 mV dec⁻¹, which is smaller than that of commercial Pt/C-RuO₂ (122 mV dec⁻¹), MCO-30%T (130 mV dec⁻¹), MCO (195 mV dec⁻¹), and MCO-50%T

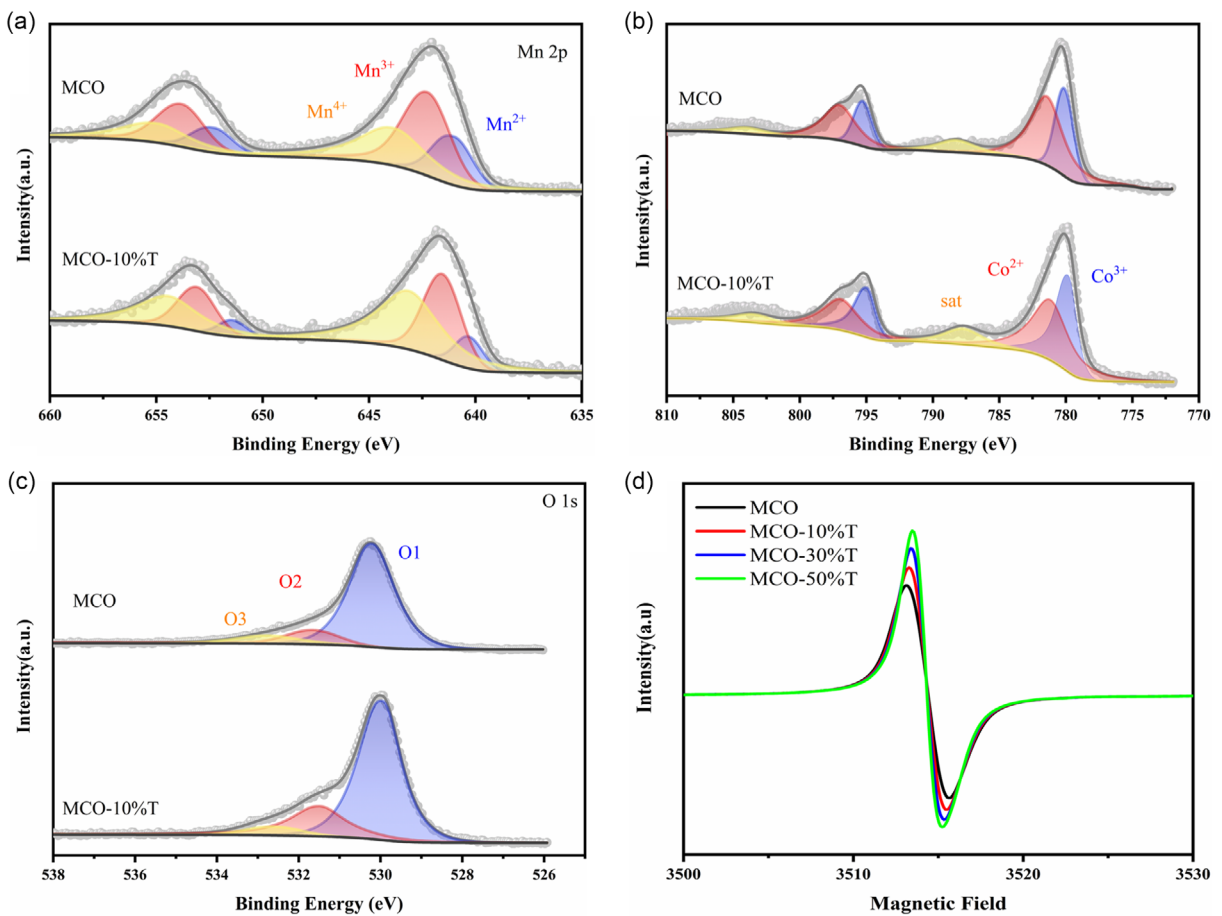


Figure 4. XPS spectra of a) Mn 2p, b) Co 2p, and c) O 1s, and d) ESR spectra of MCO and MCO-10%T.

(201 mV dec⁻¹), indicating the carbon after calcination of thiourea improved the conductivity of catalyst, thus accelerating electron transport and ORR reaction kinetics (Figure 5b).^[41] The LSV curves for MCO-10%T and commercial Pt/C-RuO₂ at varying rotation rates (225–2025 rpm) show that as the rotation rate decreases, the limiting current density also decreases (Figure S3a–d, Supporting Information), signifying that current density is influenced by dynamic factors. Figure S3e,f, Supporting Information shows that MCO-10%T has the highest number of electron transfers, electron transfer number near 4, showing that the ORR interaction in MCO-10%T follows a four-electron decrease pathway. To additionally evaluate the ORR synergist action, H₂O₂% and electron transfer quantities of MCO-10%T were estimated utilizing RRDE. Figure S4, Supporting Information shows that the electron transfer number for MCO-10%T is near 4, and the hydrogen peroxide yield is low, obviously demonstrating great selectivity for the reactant decrease of oxygen to water.^[31]

The OER performance of MCO, MCO-10%T, MCO-30%T, and MCO-50%T was analyzed using RRDE voltammetry in a 0.1 M KOH. The LSV curves in Figure 5c reveal that Pt/C-RuO₂ exhibits the lowest onset potential of 1.54 V versus RHE at a current density of 1 mA cm⁻². Notably, MCO-10%T achieves an onset potential of 1.59 V versus RHE, closely matching the performance of the commercial catalyst. In comparison, higher onset potentials are observed for MCO-50%T (1.61 V vs. RHE), MCO-30%T (1.63 V vs. RHE), and MCO

(1.68 V vs. RHE). The overpotential is another vital factor for assessing OER catalytic activity, as smaller overpotentials signify better performance.^[42] MCO-10%T presents a potential of 1.68 V (vs. RHE) at 10 mA cm⁻², which is around 20, 40, and 100 mV less than those of MCO-50%T, MCO-30%T, and MCO, respectively, and only 30 mV over Pt/C-RuO₂. Importantly, MCO-10%T exhibits the quickest rise in current density, suggesting that the additional micropores and mesopores formed during the high-temperature sublimation of thiourea enhance the kinetics of the OER reaction, a finding supported by the Tafel slope shown in Figure 5d. The Tafel slope of MCO-10%T is 81.6 mV dec⁻¹, outperforming the commercial Pt/C-RuO₂ (84.7 mV dec⁻¹), MCO-50%T (85 mV dec⁻¹), MCO-30%T (87.4 mV dec⁻¹), and MCO (96.5 mV dec⁻¹).

The Nyquist plot of all produced samples is displayed in Figure S5, Supporting Information, and the half-circle shape indicates that the charge transfer process is mostly in charge of the catalytic reaction.^[43] OER activity on the catalyst surface is increased by the MCO-10%T catalyst, which has the smallest semicircle diameter and the lowest charge transfer resistance.^[43] The Tafel slope result is consistent with this observation.

Furthermore, a favorable association has been seen between catalyst activity and active sites. The corresponding C_{dl} values, which were determined using the relevant electrocatalysts' CV curves, are displayed in Figure S6, Supporting Information. Figure 5e shows the C_{dl} value for MCO-10%T is 6.29 mF cm⁻²,

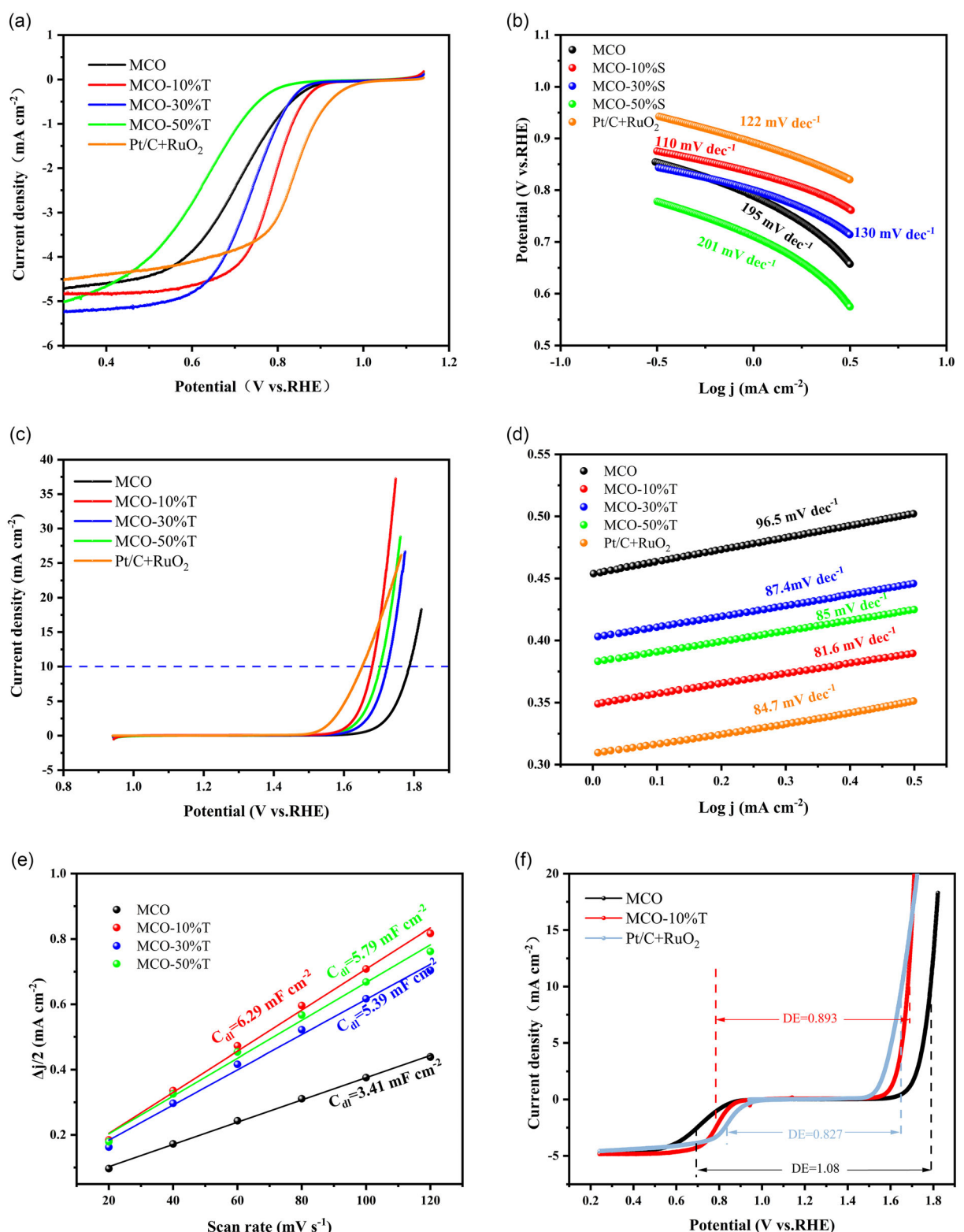


Figure 5. a) LSV curves for MCO, MCO-10%T, MCO-30%T, MCO-50%T, and Pt/C-RuO₂. b) Tafel plots of ORR c) OER curves for various catalysts. d) Tafel plots for the OER, e) C_{dl} plots for various materials. f) LSV curves for both OER and ORR.

significantly higher than that of MCO (3.41 mF cm^{-2}), MCO-30%T (5.39 mF cm^{-2}), and MCO-50%T (5.79 mF cm^{-2}). These results suggest that MCO-10%T possesses more active sites and superior OER activity. Furthermore, the ΔE value, defined as

the difference between the OER potential at 10 mA cm^{-2} ($E_j = 10 \text{ mA cm}^{-2}$) and the ORR half-wave potential ($E_{1/2}$), is 0.893 V for MCO-10%T (Figure 5f). This value is notably lower than those reported for recently studied materials (Table S4,

Supporting Information), underscoring its superior bifunctional electrocatalytic performance.

Figure 6 presents the LSV curves for the ORR and OER of MCO-10%T and MCO after 2000 cycles. Compared to MCO, the MCO-10%T sample exhibited low performance loss after 2000

CV cycles. The ORR half-wave potential of MCO-10% S decreased by only 1 mV, which is much lower than 12 mV decrease observed for MCO (Figure 6a,c). Under the OER reaction at 10 mA cm⁻², the potential of MCO increased by 65 mV, whereas the MCO-10% S sample demonstrated greater OER durability under the same

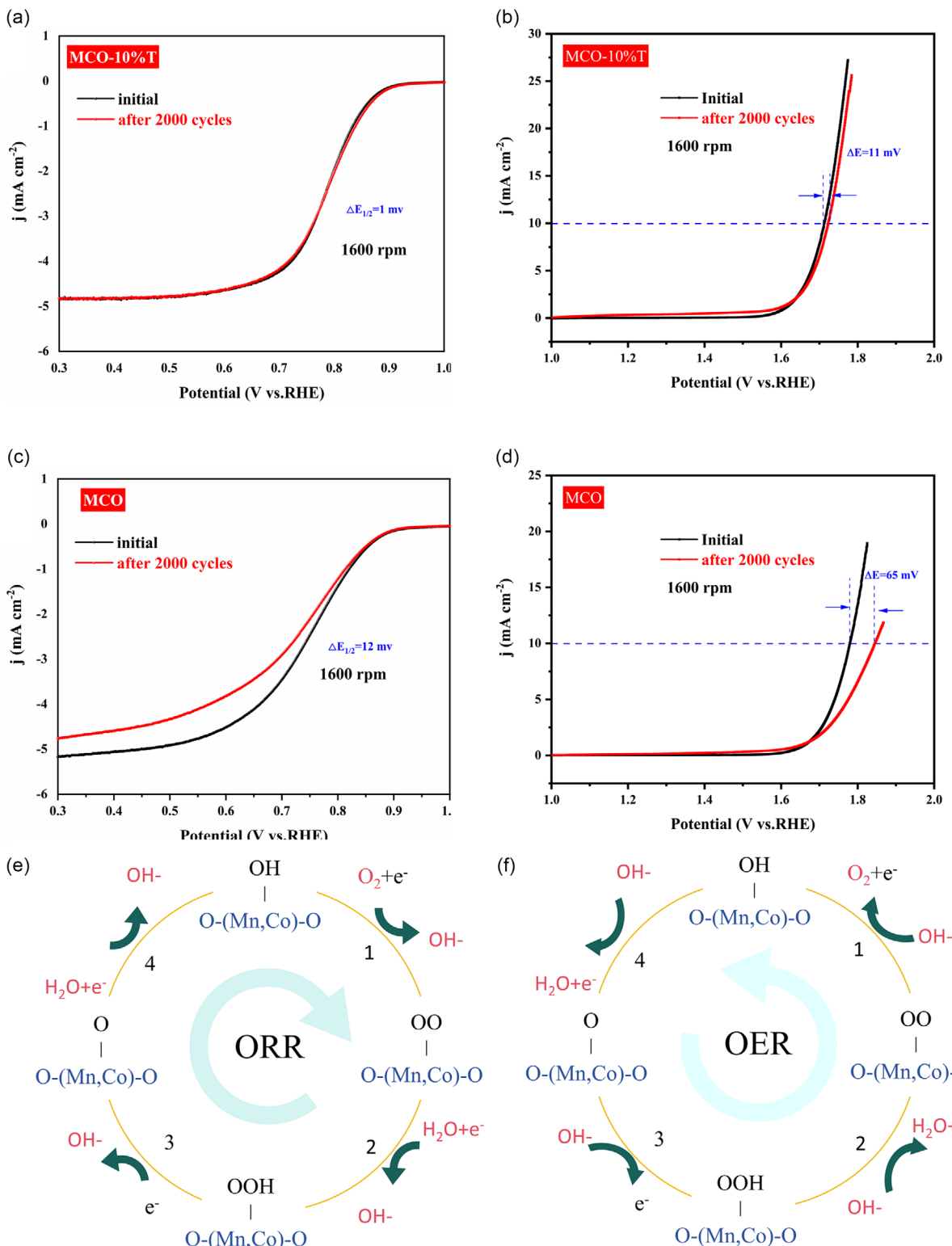


Figure 6. a,b) The stability of the MCO-10%T and MCO for ORR after 2000 cycles, c,d) The stability of the MCO-10%T and MCO for OER after 2000 cycles; e) ORR catalytic mechanism, and f) OER catalytic mechanism.

conditions, with an increase of just 11 mV (Figure 6b,d). Additionally, the catalytic mechanism of the ORR and OER processes are illustrated in Figure 6e-f, respectively. The ORR typically involves two main steps: first, O_2 adsorb onto the catalyst surface and are gradually activated through the acquisition of electrons and protons (i.e., reaction 1). In the second step, the intermediate species continue to receive electrons and protons on the catalyst surface, eventually being reduced to form water molecules (i.e., reaction 4). In contrast, the OER primarily involves the oxidation of O species to OOH species, necessitating the overcoming of a high energy barrier (i.e., reaction 3). The precise mechanisms of the ORR and OER reactions are still under investigation.

3.3. ZABs Performance

A rechargeable liquid ZABs was manufactured utilizing MCO-10%T as the air cathode material. Figure S7, Supporting Information demonstrates that the MCO-10%T-based ZABs achieve an outstanding open-circuit voltage of 1.486 V, surpassing the 1.461 V observed for MCO. Figure 7a demonstrate superior performance compared to the MCO battery, and MCO-10%T is nearly on par with the Pt/C-RuO₂ battery. Interestingly, the MCO-10%T battery's voltage gap at 60 mA cm⁻² is 1.141 V, which is marginally greater than the Pt/C-RuO₂ battery's (0.977 V) and lower than the MCO battery's (1.266 V) at the same current density. This indicates that the dual-function performance of MCO-10%T is more efficient than that of MCO. The superior activity of MCO-10%T for ORR

and OER can be linked to its unique morphology and electronic structure, which enable fast reaction kinetics.

As shown in Figure 7b, MCO-10%T-based ZABs achieve the highest maximum power density of 154 mW cm⁻², surpassing that of Pt/C-RuO₂ (118 mW cm⁻²) and MCO (112 mW cm⁻²). When accounting for zinc mass loss, the specific capacity of liquid ZABs with an MCO-10%T air cathode reaches 800 mAh g⁻¹ at a current density of 10 mA cm⁻², compared to 757 mAh g⁻¹ for MCO, demonstrating that MCO-10%T enhances zinc utilization over MCO catalysts (Figure 7c). With an initial voltage gap of 0.80 V, MCO-10%T-based ZABs exhibit a round-trip efficiency of 60.7%, with discharge and charge potentials of 1.22 and 2.01 V, respectively, at 5 mA cm⁻². After 297 cycles, the round-trip efficiency decreases slightly to 55%, and after 691 cycles, it only drops by 7% (Figure 7d). Conversely, the voltage gap of the Pt/C-RuO₂ catalyst significantly increases after just 24 h of operation. An examination of the MCO-10%T material after 200 cycles revealed that it maintained its rod-like structure, although there was a slight reduction in size. After 200 cycles, the size of the nanoparticles increased, but the nanorod structure remained, indicating that MCO-10%T had excellent stability (Figure S8, Supporting Information). Figure 7e illustrates that two liquid ZABs with MCO-10%T connected in series can stably light LED bulbs, confirming their promising potential in miniaturized devices.

At present, ZABs are predominantly utilized in compact devices such as hearing aids and various electronic applications. To better understand the practical viability of MCO-10%T, we constructed solid-state ZABs with MCO-10%T-coated carbon cloth

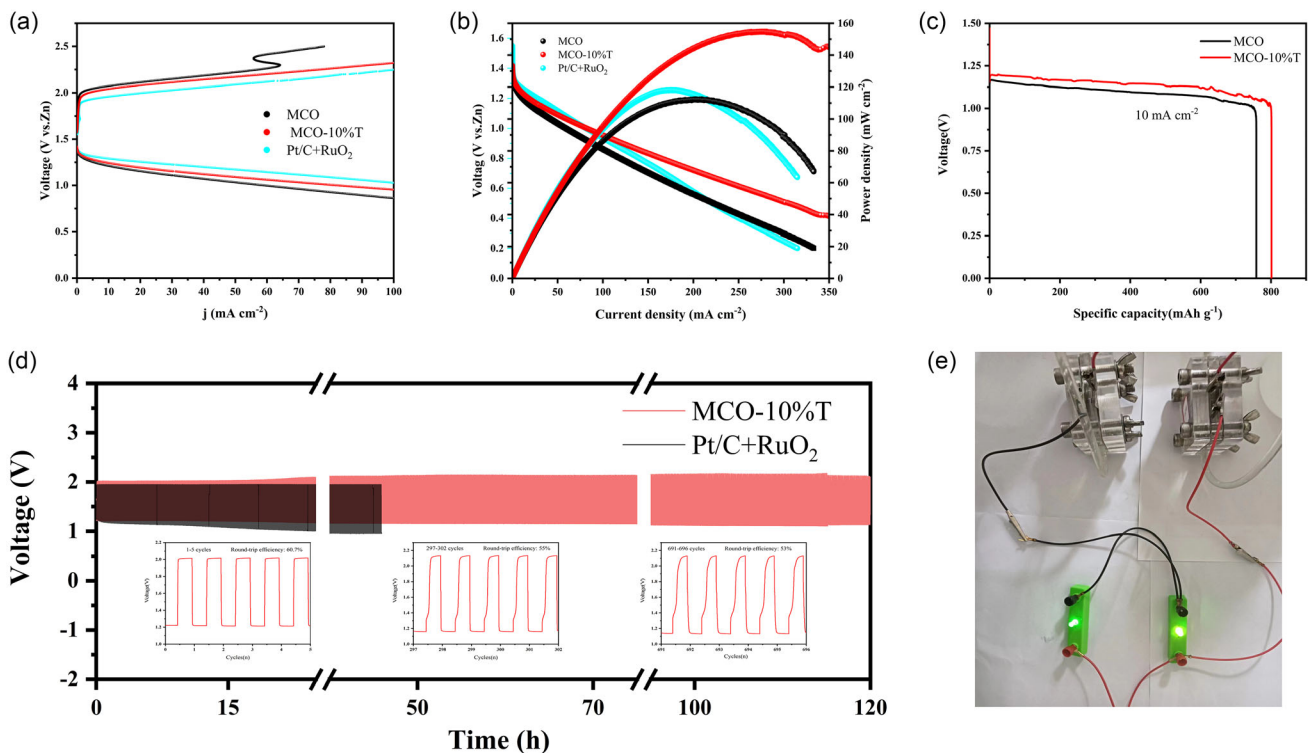


Figure 7. a) Charging-discharging polarization response; b) Polarization and power density curves; c) Specific capacity; d) Charge cycle stability at a constant discharge of 5 mA cm⁻², including illustrations of cycle performance during the initial, intermediate, and final cycles; and e) LED bulbs powered by two ZABs (MCO-10%T).

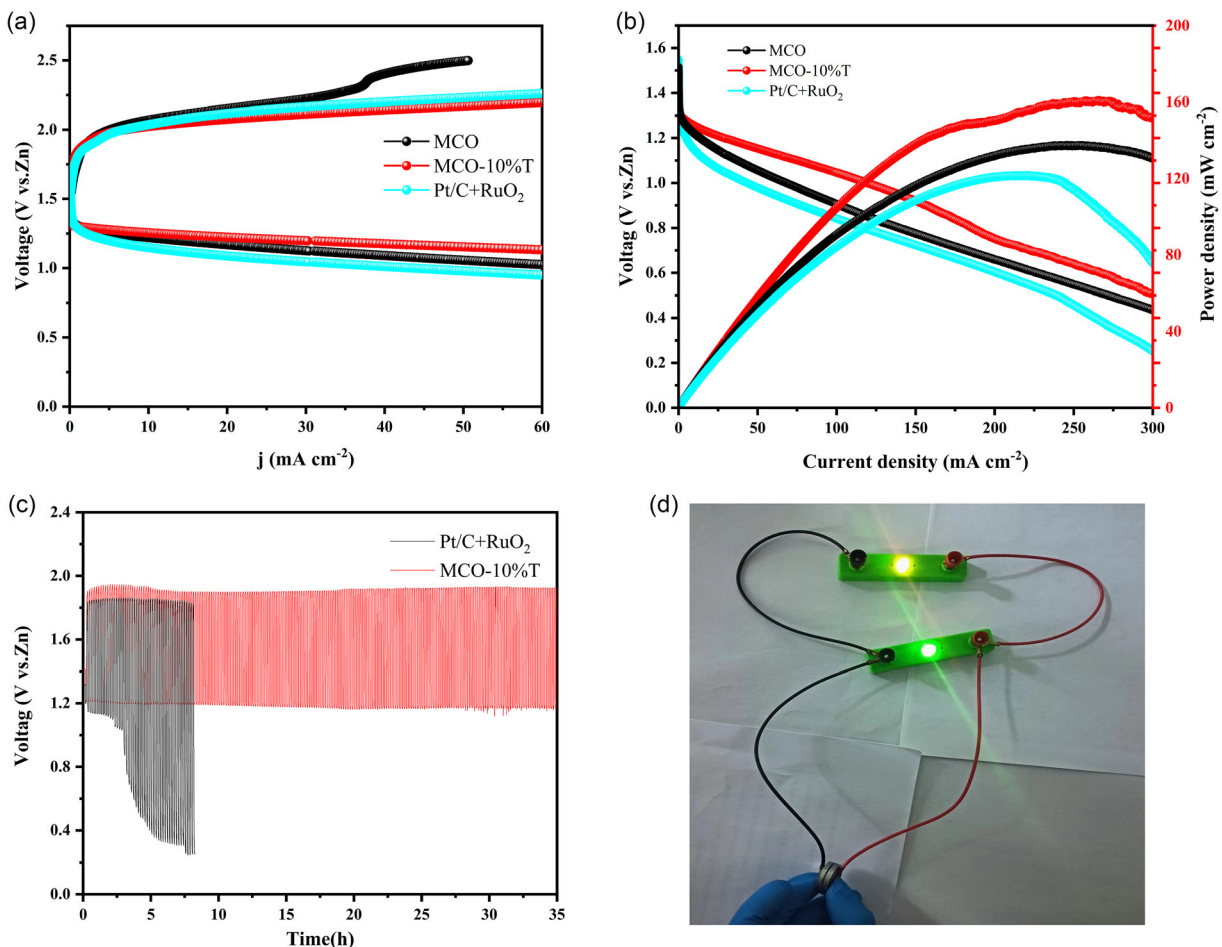


Figure 8. a) Charging–discharging polarization response; b) corresponding power density curves; c) Cycling performance of button-type ZABs; d) Two button batteries powering LED lights.

as the air cathode. Notably, MCO-10%T demonstrated superior charge–discharge performance among these solid-state batteries (Figure 8a), achieving a peak power density of 160 mW cm^{-2} , which exceeds the performance of MCO (130 mW cm^{-2}) and the commercial standard of 123 mW cm^{-2} (Figure 8b).

Additionally, Figure 8c shows that after 35 h of charge–discharge cycling, the battery based on MCO-10%T still maintained good stability, outperforming Pt/C-RuO₂. Two solid-state ZABs connected in series successfully powered an LED (Figure 8d). This strongly suggests that solid-state ZABs based on MCO-10%T have excellent practical viability.

4. Conclusion

In summary, the surface of MCO was successfully modified through a one-step, low-temperature heat treatment process. This modification introduced carbon, sulfur doping, and a significant number of surface oxygen vacancies. The custom ZAB incorporating this catalyst demonstrated a high power density of 154 mW cm^{-2} and an impressive specific capacity (800 mA h g^{-1}). The superior bifunctional properties of this catalyst can be attributed to: (1) its high specific surface area and relatively uniform pore-size distribution,

(2) the carbon, which enhances electrical conductivity and stability, and (3) the increased presence of Mn^{4+} , Co^{3+} , and oxygen vacancies. This work presents a viable approach for in-situ surface reconstruction of materials to serve as effective cathode catalysts in ZABs.

Acknowledgements

The Jiangsu Higher Education Institutions' Priority Academic Program Development (PAPD) and Top-notch Academic Programs Project (TAPP) provided funding for this project. Thanks eceshi (www.eceshi.com) for the SEM test.

Conflict of Interest

The authors declare no conflict of interest.

Data Availability Statement

Research data are not shared

Keywords: spinel · surface reconfiguration · zinc–air batteries

- [1] Y. Liu, Q. Sun, W. Li, K. R. Adair, J. Li, X. Sun, *Green Energy Environ.* **2017**, 2, 246.
- [2] G. A. Elia, K. V. Kravchyk, M. V. Kovalenko, J. Chacon, A. Holland, R. G. A. Wills, *J. Power Sources* **2021**, 481, 228870.
- [3] M. Wang, Q. Sun, Y. Liu, Z. Yan, Q. Xu, Y. Wu, T. Cheng, *Chin. J. Struct. Chem.* **2024**, 43, 100203.
- [4] Y. Y. Feng, H. C. Qi, Q. Zhang, Z. Z. Chi, S. S. Zhang, Y. Y. Cui, S. X. Li, Z. Y. Guo, L. Wang, *Batteries Supercaps* **2022**, 5, 2566.
- [5] C. Duan, R. J. Kee, H. Zhu, C. Karakaya, Y. Chen, S. Ricote, A. Jarry, E. J. Crumlin, D. Hook, R. Braun, N. P. Sullivan, R. O'Hare, *Nature* **2018**, 557, 217.
- [6] J. Chi, H. Yu, *Chin. J. Catal.* **2018**, 39, 390.
- [7] Y. Zhang, Y. Zhang, Z. Guo, Y. Fang, C. Tang, N. Miao, B. Sa, J. Zhou, Z. Sun, *J. Colloid. Interface. Sci.* **2023**, 652, 1954.
- [8] L. Tang, Y. Wan, Y. M. Lin, *Chin. J. Struct. Chem.* **2024**, 43, 100345.
- [9] S. Li, X. Hao, A. Abudula, G. Guan, *J. Mater. Chem. A* **2019**, 7, 18674.
- [10] Y. Zhou, R. Lu, X. Tao, Z. Qiu, G. Chen, J. Yang, Y. Zhao, X. Feng, K. Muellen, *J. Am. Chem. Soc.* **2023**, 145, 3647.
- [11] Y. Zhao, D. P. A. Saseendran, C. Huang, C. A. Triana, W. R. Marks, H. Chen, H. Zhao, G. R. Patzke, *Chem. Rev.* **2023**, 123, 6257.
- [12] J. Gan, J. Zhang, B. Zhang, W. Chen, D. Niu, Y. Qin, X. Duan, X. Zhou, *J. Energy Chem.* **2020**, 45, 59.
- [13] M. Ruan, J. Liu, P. Song, W. Xu, *Chin. J. Catal.* **2022**, 43, 116.
- [14] H. Park, J. Yang, M. K. Cho, Y. Lee, S. Cho, S. Yim, B. Kim, J. H. Jang, H. Song, *Nano Energy* **2019**, 55, 49.
- [15] C. Wei, Z. Feng, G. G. Scherer, J. Barber, Y. Shao-Horn, Z. J. Xu, *Adv. Mater.* **2017**, 29, 1606800.
- [16] M. Zhou, D. Yoon, Y. Yang, L. Zhang, C. Li, H. Wang, A. Sharma, S. Jiang, D. A. A. Muller, H. D. Abruna, J. Fang, *ACS Energy Lett.* **2023**, 8, 3631.
- [17] F. Cheng, J. Shen, B. Peng, Y. Pan, Z. Tao, J. Chen, *Nat. Chem.* **2011**, 3, 79.
- [18] Y. Zhu, X. Liu, S. Jin, H. Chen, W. Lee, M. Liu, Y. Chen, *J. Mater. Chem. A* **2019**, 7, 5875.
- [19] Z. Bai, J. Heng, Q. Zhang, L. Yang, F. Chang, *Adv. Energy Mater.* **2018**, 8, 1802390.
- [20] Z. Zhang, H. Sun, J. Li, Z. Shi, M. Fan, H. Bian, T. Wang, D. Gao, *J. Power Sources* **2021**, 491, 229584.
- [21] J. Ran, T. Wang, J. Zhang, Y. Liu, C. Xu, S. Xi, D. Gao, *Chem. Mat.* **2020**, 32, 3439.
- [22] X. Chen, Z. Yan, M. Yu, H. Sun, F. Liu, Q. Zhang, F. Cheng, J. Chen, *J. Mater. Chem. A* **2019**, 7, 24868.
- [23] X. Wang, Y. Li, T. Jin, J. Meng, L. F. Jiao, M. Zhu, J. Chen, *Nano Lett.* **2017**, 17, 7989.
- [24] H. Zhou, W. Zhao, J. Yan, Y. Zheng, *J. Power Sources* **2024**, 597, 234104.
- [25] Z. Lu, H. Zhou, B. Qian, S. Wang, Y. Zheng, L. Ge, H. Chen, *Int. J. Hydron. Energy* **2023**, 48, 8082.
- [26] T. Li, A. Abdelhaleem, W. Chu, S. Pu, F. Qi, J. Zou, *Chem. Eng. J.* **2021**, 411, 128450.
- [27] M. Usman, A. Ahmed, Z. Ji, B. Yu, M. Rafiq, Y. Shen, H. Cong, *Mater. Today Chem.* **2022**, 26, 101003.
- [28] A. Misra, P. K. Tyagi, M. K. Singh, D. S. Misra, *Diam. Relat. Mat.* **2006**, 15, 385.
- [29] L. Liu, H. Huang, J. Tai, X. Wu, Z. Guo, X. Shen, S. Cui, X. Chen, *Carbon* **2024**, 219, 118847.
- [30] R. S. Kumar, S. Prabhakaran, S. Ramakrishnan, S. C. Karthikeyan, A. R. Kim, D. H. Kim, D. J. Yoo, *Small* **2023**, 19, 20.
- [31] X. Li, B. Y. Guan, S. Gao, X. Wen, *Energy Environ. Sci.* **2019**, 12, 648.
- [32] X. Li, D. C. Nguyen, K. Dong, S. Prabhakaran, D. T. Tran, D. H. Kim, N. H. Kim, J. H. Le, *Chem. Eng. J.* **2024**, 489, 151210.
- [33] H. Ren, H. Li, H. Fan, G. Qi, Y. Liu, *Sep. Purif. Technol.* **2023**, 305, 122472.
- [34] S. T. Wang, Y. Liu, X. P. Liu, Y. Chen, Y. L. Zhao, S. Y. Gao, *ChemistrySelect* **2022**, 7, e202200044.
- [35] P. Gayen, S. Saha, K. Bhattacharyya, V. K. Ramani, *ACS Catal.* **2020**, 10, 7734.
- [36] L. An, Y. Hu, J. Li, J. Zhu, M. Sun, B. Huang, P. Xi, C. Yan, *Adv. Mater.* **2022**, 34, 2202874.
- [37] J. Li, X. He, Y. Du, M. Jiang, Q. Hu, J. Yin, F. Yang, J. Zhang, *Chem. Eng. J.* **2023**, 475, 146183.
- [38] S. Wang, S. Liu, X. Chen, Y. Guo, X. Xu, L. Yang, Y. Zhao, C. Chen, H. Liang, R. Hao, *Chem. Eng. J.* **2023**, 453, 139901.
- [39] S. Alkhalaf, C. K. Ranaweera, P. K. Kahol, K. Siam, H. Adhikari, S. R. Mishra, F. Perez, B. K. Gupta, K. Ramasamy, R. K. Gupta, *J. Alloy. Compd.* **2017**, 692, 59.
- [40] M. Wu, B. Guo, A. Nie, R. Liu, *J. Colloid. Interface. Sci.* **2020**, 561, 585.
- [41] M. Wang, Q. Sun, Y. Liu, Z. Yan, Q. Xu, Y. Wu, T. Cheng, *Adv. Funct. Mater.* **2025**, 2425640, <https://doi.org/10.1002/adfm.202425640>.
- [42] J. O. Olowoyo, R. J. Kriek, *Small* **2022**, 18, 2203125.
- [43] G. Abrham Gebreslase, M. Victoria Martinez-Huerta, M. Jesus Lazaro, *J. Energy Chem.* **2022**, 67, 101.

Manuscript received: February 20, 2025

Revised manuscript received: April 11, 2025

Version of record online: April 28, 2025